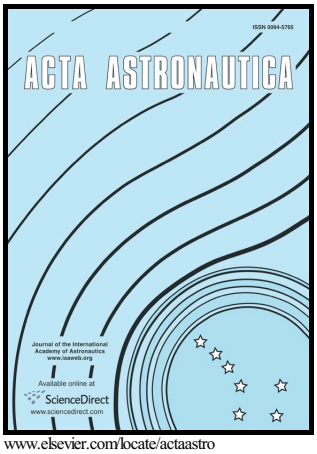

www.elsevier.com/locate/actaastro

Pressure oscillations and instability of working processesin the combustion chambers of solid rocket motors

V.N. Emelyanov, I.V. Teterina, K.N. Volkov, A.U. Garkushev

PII: S0094-5765(16)30815-3
DOI: http://dx.doi.org/10.1016/j.actaastro.2016.09.029
Reference: AA6018

To appear in: *Acta Astronautica*

Received date: 18 August 2016
Revised date: 24 September 2016
Accepted date: 27 September 2016

Cite this article as: V.N. Emelyanov, I.V. Teterina, K.N. Volkov and A.U. Garkushev, Pressure oscillations and instability of working processesin th combustion chambers of solid rocket motors, *Acta Astronautica* http://dx.doi.org/10.1016/j.actaastro.2016.09.029

Pressure oscillations and instability of working processesin the combustion chambers of solid rocket motors

V.N. Emelyanov[1], I.V. Teterina[1], K.N. Volkov[2], A.U. Garkushev[3]

[1]Faculty of Rocket and Space Engineering, Baltic State Technical University,
190005, St. Petersburg, Russia
[2]Faculty of Science, Engineering and Computing, Kingston University,
SW15 3DW, London, United Kingdom
[3]Institute of Military Engineering and Safety Research,
Peter the Great St. Petersburg Polytechnic University, 195251, St. Petersburg, Russia

Abstract
Metal particles are widely used in space engineering to increase specific impulse and to supress acoustic instability of intra-champber processes. A numerical analysis of the internal injection-driven turbulent gas-particle flows is performed to improve the current understanding and modeling capabilities of the complex flow characteristics in the combustion chambers of solid rocket motors (SRMs) in presence of forced pressure oscillations. The two-phase flow is simulated with a combined Eulerian–Lagrangian approach. The Reynolds-averaged Navier–Stokes equations and transport equations of $k-\varepsilon$ model are solved numerically for the gas. The particulate phase is simulated through a Lagrangian deterministic and stochastic tracking models to provide particle trajectories and particle concentration. The results obtained highlight the crucial significance of the particle dispersion in turbulent flowfield and high potential of statistical methods. Strong coupling between acoustic oscillations, vortical motion, turbulent fluctuations and particle dynamics is observed.

Keywords
Solid rocket motor; Acoustic intability; Injection-driven flow; Two-phase flow; Particle; Turbulence; Dispersion

1 Introduction

High-energy rocket propellants are the mixtures of fuel, oxidiser and metal particles. These propellants contain high explosives that can detonate under high shock loads, high temperatures and other conditions. In particularly, pressure oscillations in the combustion chamber significantly affect intra-chamber processes and combustion instability.

Aluminum particles in solid propellants serve two purposes, increasing specific impulse and suppressing high-frequency combustion instability. Unlike the other ingredients, aluminum particles burn in a significant portion of the combustion chamber of solid rocket motor (SRM) and produce alumina smoke and agglomerates that are carried out into the flowfield [1]. The presence of aluminum droplets in the flowfield contributes to the motor performance loss through decreasing nozzle efficiency and surface damage from droplet impingement. Detailed knowledge of particulate phase characteristics as residue size, burning time and heat release as well as particle dynamics and particle dispersion in a turbulent flowfield are essential to improve motor performance and reliability and to ensure safety.

Accurate prediction of the turbulent two-phase flowfield is of great importance to the correct estimation of performance of SRM and slag accumulation rate. An analysis is hampered by the complex flow features involving complex geometry, turbulence with mass injection, recirculation regions, a wide range of Mach numbers, two-phase flow phenomena, heterogeneous combustion, and

uncertainties in particle density and particle size distribution (Figure 1).

Turbulence plays an important role in determining the wave properties through the damping effect of turbulence-induced eddy viscosity on vortical motion. Turbulence modeling becomes necessary for the evaluation of heat transfer and related phenomena (e.g. erosive burning). The interactions between organized oscillatory motions and turbulent fluctuations give rise to additional mechanisms of energy production, transfer and dissipation of wave modes. The difficulty in simulation of turbulence comes from the fact the transition is always inside the SRM, since the velocity at the head-end is equal to zero.

Erosive burning represents an increase of the local propellant burning rate due to high velocity combustion gas flow across the burning surface. Erosive burning mechanism is due to increase in gas to solid heat feedback caused by the increase in transport coefficients, and turbulence enhanced mixing and chemical reaction of the oxidizer and fuel rich gases pyrolized for composite propellant.

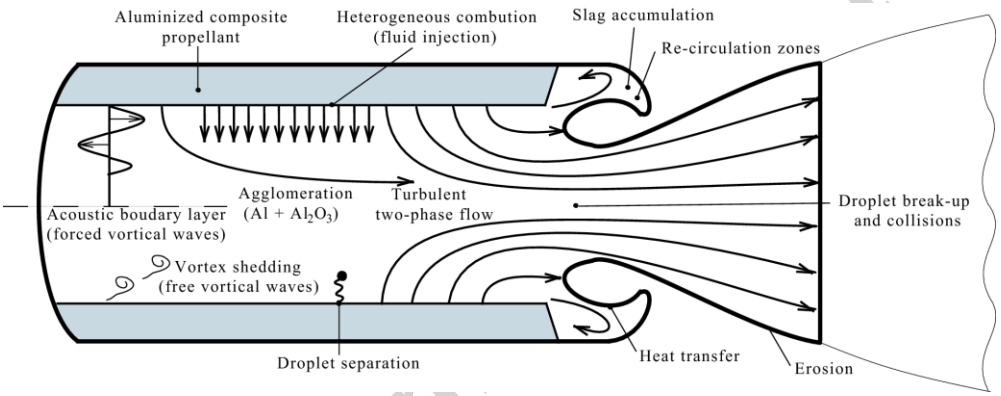

Figure 1. Combustion chamber

Aluminum droplet combustion and alumina residue behavior in the combustion chamber of SRMs affect combustion instabilities by acting as driving or damping mechanisms [2]. Some of aluminum droplets remain in the motor during its operation and collect in the aft-end region. Inside the motor, these droplets are the source of slag material. Alumina slag deposition at motor aft-end results in motor performance loss, damage of thermal protection due to overheating, and possible sloshing and ejection of liquid agglomerates through the nozzle, which may cause pressure disturbances and trust imbalance.

SRMs are subject to pressure oscillations caused by vortex shedding and acoustic feedback resulting from impingement of the vortices on the nozzle and other obstacles [3–9]. The oscillatory flowfield in a SRM consists of three distinct types of wave motions: acoustic (irrotational and compressible), vortical (rotational and incompressible) and entropy (arising from unsteady heat release) modes [10]. The coupling between the acoustic wave and the incoming radial mass flow from the propellant surface generates fluctuating vorticity and causes the energy transfer from the acoustic to the vortical field (flow-turning energy losses) [3, 4]. The interactions between entropy fluctuations and non-uniform flow act as a strong source term for driving acoustic oscillations in regions with large velocity gradients [3, 11]. The three waves, along with the transient combustion response of propellant, dictate the stability behavior of SRMs.

In many cases, the stability of intra-chamber processes in SRMs is studied within the framework of the linear theory and acoustic balance methods ignoring interaction of acoustic and vortex motions [3, 4].

Two-phase flows with inert and burning aluminum particles as well as the influence of particles on acoustic oscillations in the combustion chamber are considered in [2, 12–15], where the results of numerical simulations based on the Eulerian–Eulerian and Eulerian–Lagrangean approaches and some experimental results are reported.

Two mechanisms are responsible for attenuation of acoustic oscillations in the combustion chamber [2]. First, the acoustic energy is transferred to and dissipated by particles through the momentum and heat exchange in the two-phase flow. Second, the acoustic energy balance is substantially modified by the distributed combustion of particles.

Flow oscillations are expected to interact with the agglomeration process on the burning surface (mechanism 1), with the ignition and the distributed combustion that may occur in a significant portion of the combustion chamber (mechanism 2) and with alumina residues in the entire volume of the chamber (mechanism 3). The first and the third interactions are identified as damping phenomena while the second is suspected to be a driving mechanism. Their effectiveness depends on oscillation frequencies, droplet sizes and burning-to-residence time ratio. Net contribution of aluminum to the global acoustic balance may be positive or negative [2, 3, 5].

At high frequencies, particles usually exert a damping effect on acoustic oscillations [2], and suppression of oscillations occurs due to the influence of agglomerates on the fluctuations on the burning surface (mechanism 1). At frequencies below 2000 Hz, mechanism 1 plays a minor role as compared to mechanism 3, but this interaction also leads to damping of oscillations. Some propellants that ensure stable combustion without metallic particles display a tendency to combustion instability due to addition of aluminum, which is caused by the influence of mechanism 2, which leads to enhancement of oscillations [16].

Theoretical relations and semi-empirical correlations for calculating the dependence of the attenuation and dispersion coefficients of acoustic oscillations on the particle size and thermo-physical properties of the gas and particles are presented in [17].

In order to extend the reliability of numerical calculations as a predicting tool to be used for industrial applications in design and development of SRMs, one needs to improve the level of accuracy of physical models and the effectiveness of numerical schemes. The study focuses on the development of numerical analysis of the internal two-phase flows with emphasis on the momentum and energy transfer between the gas and particles in presence of forced pressure oscillations, particle dynamics and particle dispersion in turbulent flowfield, interaction between turbulent and forced oscillatory flowfields, and effects of particles on steady and unsteady flow motions. In contrast to models reported in [2, 15], the motion of particulate phase in a turbulent flow is simulated with a stochastic tracking model [18] taking into account the coupling between turbulence, vortical flowfield and particle dynamics.

2 Mathematical model

The two-phase flow is simulated with a combined Eulerian–Lagrangian approach. The unsteady Reynolds-averaged Navier–Stokes equations (RANS) are solved numerically for the gas phase. The particulate phase is simulated through a Lagrangian deterministic or stochastic tracking models to provide particle trajectories and particle concentration [18].

2.1 Gas

Combustion takes place near the propellant surface with a typical flame height of tens to hundreds of microns. Flow study considers the flow of a non-reactive mixture of combustion products. Aluminum particles burn near the the propellant surface. The particles are treated as non-deformable and non-rotating spheres of an identical size. Collisions, fragmentation and coagulation of particles are ignored. Particle collisions become important if the range of particle sizes is sufficiently large [2].

Due to hard conditions inside the combustion chamber ($p > 1$ MPa and $T > 2600$ K) and the relative short durations of the propellant burn, measurements are difficult in such unfriendly conditions. Flow simulation based on cold air injection through channel surface presents many advantages. For the cold flow, chemical reactions are not included to allow for a detailed investigation of flow dynamics without complications arising from the surface and distributed combustion of propellant and aluminum particles.

As the propellant burns, the combustion chamber geometry continuously changes. However, due to high density ratios of solid propellant and combustion products (typical density ratio of solid and gas phases is more than 1000), the propellant regression rate is three orders of magnitude smaller that gas velocities. It permits to uncouple the two mechanisms, and the entire burn is represented by a succession of fixed geometries in which the flow solution is computed.

The governing equations of gas represent the conservation equations of mass, momentum and energy in Cartesian coordinates. The x axis is aligned with the centreline of the channel, and the y axis is aligned with the radius. The injection velocity, v_w, is assumed to be identical at all points of the propellant surface and to be directed normal to this surface. The parameters of the gas and particles entering the channel are assumed to be constant along the burning surface. Aluminum particles are injected from the surface of the channel at points uniformly distributed over the channel length.

In Cartesian coordinates (x, y, z), an unsteady three-dimensional flow of a viscous compressible gas is described by the following equations

$$\frac{\partial \rho}{\partial t} + \nabla \cdot (\rho \mathbf{v}) = 0; \tag{1}$$

$$\frac{\partial \rho \mathbf{v}}{\partial t} + \nabla \cdot (\rho \mathbf{v}\mathbf{v}) = -\nabla p + \nabla \cdot \tau - \sum_i \mathbf{F}_{\mathrm{p}i} n_{\mathrm{p}i}; \tag{2}$$

$$\frac{\partial \rho e}{\partial t} + \nabla \cdot [(\rho e + p)\mathbf{v}] = -\nabla \cdot \mathbf{q} + \nabla \cdot (\tau \cdot \mathbf{v}) - \sum_i W_{\mathrm{p}i} n_{\mathrm{p}i} - \sum_i Q_{\mathrm{p}i} n_{\mathrm{p}i}. \tag{3}$$

The equation of state of an ideal gas is

$$p = (\gamma - 1)\rho \left[e - \frac{1}{2}\left(v_x^2 + v_y^2 + v_z^2\right) \right].$$

Here, t is the time, ρ is the density, v_x, v_y, and v_z are the velocity components in the coordinate directions x, y and z, p is the pressure, e is the total energy per unit mass, T is the temperature, and γ is the specific heat capacity ratio. The subscript p corresponds to the particles. Summation is performed over all particles of the ith fraction.

The viscous stress tensor and the heat flux vector are related to the velocity and temperature fields by the relations

$$\tau = \mu_e [\nabla \mathbf{v} + (\nabla \mathbf{v})^*], \quad \mathbf{q} = -\lambda_e \nabla T,$$

where μ_e is the effective viscosity and λ is the effective thermal conductivity. The adjoint tensor is

indicated by the asterisk.

The equations (1)–(3) are suitable for both laminar and turbulent flows. For turbulent flow, the effective viscosity, μ_e, is calculated as the sum of molecular viscosity, μ, and turbulent eddy viscosity, μ_t, and the effective thermal conductivity, λ_e, is expressed in terms of effective viscosity and Prandtl number

$$\mu_e = \mu + \mu_t, \quad \lambda_e = c_p\left(\frac{\mu}{\mathrm{Pr}} + \frac{\mu_t}{\mathrm{Pr}_t}\right),$$

where c_p is the specific heat capacity at constant pressure, and $\mathrm{Pr} = 0.72$ and $\mathrm{Pr}_t = 0.9$. The eddy viscosity is calculated by the Kolmogorov–Prandtl relationship ($\mu_t = c_\mu \rho k^2/\varepsilon$).

The Sutherland's law is used to calculate molecular viscosity as a function of temperature

$$\frac{\mu}{\mu_*} = \left(\frac{T}{T_*}\right)^{3/2}\frac{T_* + S_0}{T + S_0},$$

where $\mu_* = 1.68 \times 10^{-5}$ kg/(m·s), $T_* = 273$ K and $S_0 = 110.5$ K for air.

The transport equations of the turbulent kinetic energy, k, and its dissipation rate, ε, are written in the form

$$\frac{\partial \rho k}{\partial t} + (\rho \mathbf{v}\cdot\nabla)k = \nabla\left[\left(\mu + \frac{\mu_t}{\sigma_k}\right)\nabla k\right] + P - \rho\varepsilon + E_\mathrm{p}; \tag{4}$$

$$\frac{\partial \rho \varepsilon}{\partial t} + (\rho \mathbf{v}\cdot\nabla)\varepsilon = \nabla\left[\left(\mu + \frac{\mu_t}{\sigma_\varepsilon}\right)\nabla \varepsilon\right] + \frac{\varepsilon}{k}(c_{\varepsilon 1}P - c_{\varepsilon 2}\rho\varepsilon) + \Phi_\mathrm{p}. \tag{5}$$

Here, P is the turbulent generation term. The Kato–Launder correction to the turbulence generation term is applied

$$P = \mu_t |S|^{1/2}|\Omega|^{1/2}.$$

The invariants of the strain rate tensor and the rotation rate tensor are found from the relations

$$|S| = (2S_{ij}S_{ij})^{1/2}, \quad |\Omega| = (2\Omega_{ij}\Omega_{ij})^{1/2},$$

where

$$S_{ij} = \frac{1}{2}\left(\frac{\partial v_i}{\partial x_j} + \frac{\partial v_j}{\partial x_i}\right), \quad \Omega_{ij} = \frac{1}{2}\left(\frac{\partial v_i}{\partial x_j} - \frac{\partial v_j}{\partial x_i}\right).$$

The source terms in the right hand sides of equations (2) and (3) take into account the exchange of momentum between the phases, the heat transfer between the gas and the particles, and the work done by the particles on gas. The intensities of momentum and energy exchange between the phases are determined as the product of the number concentration of the particles and the intensity of interphase exchange per one particle ($n_{\mathrm{p}i}$ is the concentration of the particles of the ith fraction per unit volume). The work done by the particles on gas is calculated as $W_\mathrm{p} = \mathbf{F}_\mathrm{p}\cdot\mathbf{v}_\mathrm{p}$.

The source terms E_p and Φ_p in the equations of k–ε model (4) and (5) take into account the effect of particulate phase on turbulence (turbulence modulation).

The constants of the turbulence models are usually chosen through comparisons of calculated and experimental data obtained with steady state conditions. The applicability of the available turbulence models for the description of unsteady flows is not obvious. The data obtained in [19] show that the ratio of the shear stresses to the turbulence intensity remains approximately constant and equal to the corresponding value in a steady state flow, despite the fact that the turbulence intensity and the

components of the Reynolds stress tensor are appreciably changed in the presence of external forced pressure oscillations. At small frequencies of forced oscillations, the use of turbulence models calibrated for the steady state case seems to be justified and acceptable. If the amplitude and frequency of oscillations exceed threshold, it becomes important to take into account turbulence field interaction with external oscillations, and the traditional turbulence models become inapplicable [20]. Forced pressure oscillations affect the internal region of the boundary layer. The external part of the boundary layer behaves in the same manner as in the steady state flow [10].

It is assumed that flow unsteadiness caused by external pressure oscillations exerts a minor effect on the flow core. For modelling the flow core, equations (4) and (5) are used. The model constants are assigned the following values: c_μ=0.09, σ_k=1.0, σ_ε=1.3, $c_{\varepsilon 1}$=1.44, $c_{\varepsilon 2}$=1.92. Near the wall (in the internal region of the boundary layer), the$k$–ε turbulence model is used. The turbulent kinetic energy is found from equation (4). The dissipation rate is calculated by using an algebraic dependence with allowance for the influence of flow unsteadiness on the turbulence scale [21], rather than by means of numerical integration of equation (5).

2.2 Particulate phase

Metal particles usually appear as liquid droplets in the high-temperature environment of a combustion chamber. Particles are assumed to have a spherical shape and they are non-rotating. Particles collisions caused by acoustic oscillations and turbulent dispersion, breakup and coalescence are neglected.

The estimations show that the drag force is the main factor affecting the particle motion. The ratio of the drag force to the virtual mass force has the order $f_m/f_\mathrm{D}\sim\rho/\rho_\mathrm{p}$, and the ratio of the drag force to the Basset force has the order $f_B/f_\mathrm{D}\sim(\rho/\rho_\mathrm{p})^{1/2}$. For the aluminum particles ($\rho_\mathrm{p} = 2600$ kg/m^3) in air ($\rho = 1.25$ kg/m^3), the influence of the virtual mass force and the Basset force is neglected because they are small as compared to the drag force. The ratio of the Magnus force to the Saffman lift force has the order $\left|\boldsymbol{\omega}_\mathrm{p}\right|d_\mathrm{p}^2/(24\nu)$ and $d_\mathrm{p}^2\nu(du/dy)^{1/2}C_L$, where $\boldsymbol{\omega}_\mathrm{p}$ is the particle angular velocity, du/dy is the fluid velocity gradient, and C_L is the lift force coefficient. The Magnus force for particle diameters of $d_\mathrm{p} < 400\,\mu$m does not exceed the Saffman lift force ($f_M < f_L$), which is comparable with the drag force or greater than the latter one in high-gradient flows ($\frac{f_L}{f_D}\sim 0-10$). In low-gradient flows, such as injection-driven flows, the influence of the lift force is neglected.

The particulate phase is simulated through a Lagrangian deterministic or stochastic tracking models to provide particle trajectories [12–14, 18]. The virtual mass and Basset forces due to their small magnitudes, and the Magnus force due to lack of knowledge about particle angular momentum are neglected. The resulting force acting on a particle is the drag force. The equations describing translational motion and convective heat transfer of a spherical particle in a turbulent flowfield are written in the form

$$\frac{d\mathbf{r}_\mathrm{p}}{dt} = \mathbf{v}_\mathrm{p};$$

(6)

$$\frac{d\mathbf{v}_\mathrm{p}}{dt} = \frac{3C_\mathrm{D}\rho}{8\rho_\mathrm{p}r_\mathrm{p}}\left|\mathbf{v}-\mathbf{v}_\mathrm{p}\right|\left(\mathbf{v}-\mathbf{v}_\mathrm{p}\right);$$

(7)

$$c_\mathrm{p}^m m_\mathrm{p}\frac{dT_\mathrm{p}}{dt} = 2\pi r_\mathrm{p}\mathrm{Nu}_\mathrm{p}\lambda\left(T-T_\mathrm{p}\right).$$

(8)

To calculate the drag coefficient, the modified Stokes law is used

$$C_{\mathrm{D}} = \frac{24}{\mathrm{Re_p}} f_{\mathrm{D}}(\mathrm{Re_p}).$$

The function f_{D} takes into account the correction to the Stokes law for the particle inertia. The particle Reynolds number is

$$\mathrm{Re_p} = \frac{2r_{\mathrm{p}}\rho|\mathbf{v} - \mathbf{v}_{\mathrm{p}}|}{\mu}.$$

The particle Nusselt number is calculated based on semi-empirical correlation for solid sphere

$$\mathrm{Nu_p} = 2 + C\mathrm{Re_p}^m \mathrm{Pr}^n.$$

An important factor in particle interaction with acoustic oscillations is the ratio of dynamic and thermal particle relaxation times and the characteristic time of acoustic oscillations [15] (acoustic Stokes number). The dynamic and thermal particle relaxation times are calculated by the relations

$$\tau_v = \frac{\rho_{\mathrm{p}} d_{\mathrm{p}}^2}{18\rho\nu}, \quad \tau_t = \frac{\rho_{\mathrm{p}} c_{\mathrm{p}}^m d_{\mathrm{p}}^2}{12\rho c_p a},$$

where $a = \lambda/\rho c_p$ is the thermal diffusivity.

The fluid velocity in equation (7) represents a random function of the Cartesian coordinates and time. The fluid velocity is a sum of the averaged velocity, $<\mathbf{v}>$, and the random velocity, $\mathbf{v}'$. The averaged velocity is found from the solution of RANS equations (1)–(3). The turbulence is taken into account by introducing random velocity fluctuations into equation (7). The particles are assumed to interact with a succession of turbulence eddies, as they move through the computational domain [18]. The duration of interaction between an eddy and a particle is determined as the smaller one between the eddy life-time and the transit time required for a particle to transverse the eddy.

Equations (6)–(8) are integrated along the path of an individual particle and require specification of the initial conditions — the Cartesian coordinates and velocity of a particle at the time $t = 0$ (on the propellant surface).

3 Numerical method

The calculations are performed with the in-house CFD code developed for aerospace and related applications. The details of the code are described in [22, 23].

Flow solution is provided using cell-centered finite volume formulation of the unsteady three-dimensional compressible RANS equations on structured or unstructured meshes. Governing equations are solved by the firth step Runge–Kutta time marching scheme. Piecewise parabolic method (PPM) and Chakravarthy–Osher scheme [24] are applied to inviscid fluxes, and central difference scheme of the second order is applied to viscous fluxes. For the injection-driven flows, the fluid velocity in the bulk of the computational domain is much smaller than the acoustic speed. The conventional numerical algorithms developed for compressible flows encounter disparity of the eigenvalues of the Jacobian and singular behavior of the pressure gradient in the momentum equation. Block-Jacobi preconditioning technique and dual time-stepping integration scheme are employed to stabilize numerical calculations [25]. The numerical scheme is efficient and robust over a wide range of Mach numbers.

To solve the Cauchy problem for particle equations, the fourth-order Runge–Kutta method and methods that permit resolving in the solution rapidly and slowly decaying components are used. To supply fluid parameters at points lying in the particle trajectory, the bi-linear interpolation method is

employed. The integration time step along each trajectory is limited to the time and space turbulence scales. In the calculations, from 1000 to 10,000 trajectories of sample particles depending on their size are modelled.

The unsteady calculations are performed in the following manner. After convergence toward a steady state solution, the channel flow is excited close to its first longitudinal mode by means of one period of head-end forcing. Pressure oscillations equal to 5% of the head-end mean pressure at imposed acoustic frequencies are forced at the head-end in order to analyze unsteady flowfield. Then, the response of the flowfield to that perturbations is analyzed in terms of frequency and exponential damping.

An unstable shear layer in the mean flow produces vortices which are convected downstream to the head of the nozzle. The acoustic wave generated moves back upstream since the flow in the channel is subsonic. It perturbs the unstable shear layer, intensifying the generation of vortices. Aero-acoustic coupling leads to high amplitude fluctuations when the underlying frequency is close to the frequency of an acoustic mode. Another instability mechanism relying on the intrinsic hydrodynamic instability of the boundary layer which develops over the propellant burning surface also leads to significant pressure oscillations [26]. The first and second acoustic modes are excited during SRM operation, however the first is the stronger one.

Computations of the two-phase flow are performed in non-coupled manner and fully coupled manner. In coupled calculations, the source terms accounting for two-phase interactions are updated at every iteration. The fourth step Runge–Kutta method is applied to simulation of dynamics of large particles, and semi-analytical schemes are used for small particles. The physical time step for the particle calculations is less than 1/10 of the momentum relaxation time.

Code validation is obtained from analytical results and linear acoustic balance results [27]. The two-phase flow solver is able to describe acoustic wave damping in particle-laden flows. Parametric studies of the fluid injection velocity, particle loading and particle diameter (particle Stokes number) are performed.

4 Geometry and mesh

The physical model consists of axisymmetric channel with a closed head-end (Figure 2). Length of channel is $L = 1.88$ m, and its radius is $h = 0.2$ m. The pre-mixed gas and aluminum particles are uniformly injected from the channel walls at a stagnation pressure of 10^5 Pa and a stagnation temperature of 300 K to simulate the evolution of combustion products of solid propellant.

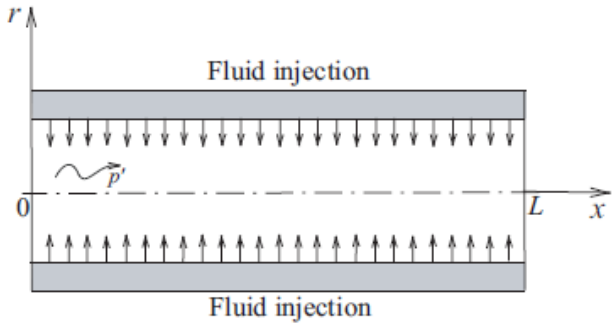

Figure 2. Geometry of channel

The air flow rate is 20 kg/(m·s) that corresponds to the propellant burning rate of 10 mm/s and density

of 2296 kg/m^3. The Mach numbers based on the surface injection velocity is about 0.002. Periodic pressure oscillations with an amplitude of 5% of the mean pressure are imposed at the channel head-end to generate longitudinal standing acoustic waves in the computational domain. On the injection wall ($r = h$), the velocities of the gas and particulate phase are subjected to the normal injection conditions ($u = u_{\mathrm{p}} = 0,\ v = v_{\mathrm{p}} = -\varphi v_{\mathrm{w}}$, where φ takes into account initial dynamic non-equilibrium of the phases, $\varphi = 0.01$). No-slip and no-penetration boundary conditions are applied to the wall. The temperature of the wall is fixed. Non-reflecting boundary conditions are applied to the channel outlet to allow for traveling acoustic waves in the channel.

A limited number of injection points located on the channel surface are considered. The particles are distributed following a uniform law. Three different particle diameters are considered (10, 20 and 100 μm).

The computational mesh consists of 400 nodes in the axial direction, and 100 nodes in the radial direction. The mesh nodes are clustered near the injection surface to resolve the vortical wave structure and turbulent boundary layer. The smallest mesh step size near the channel walls corresponds to $y^+ \sim 5$, and each vortical wavelength is covered by 10 nodes.

5 Results and discussion

The numerical model is applied to simulate internal gas-particle flow focusing on the influence of the turbulence effects on the flow structure, particle trajectories and particle dispersion, and impact of particles on vortical and acoustic flowfields. Computations of the two-phase flow are performed in non-coupled manner and fully coupled manner.

5.1 Flow structure

In the unsteady case, the flow structure near the wall is rather complicated and testifies to the presence of an acoustic boundary layer inside which there are velocity fluctuations induced by propagation of unsteady shear waves (vorticity waves) [3, 5]. Vorticity perturbations are formed due to injection from the surface owing to the no-slip conditions on the wall, propagate inward the channel, and are damped by viscous effects. In the flow core, there is a one-dimensional distribution of the axial velocity fluctuations, which is accurately described by the existing linear theory [3]. The influence of viscosity on propagation of vorticity waves is proportional to the frequency of oscillations. Flow turbulence leads to more appreciable damping of the amplitude of the axial velocity fluctuations because of additional generation of eddy viscosity.

The overall flow development is described by three distinct regimes as shown in the Figure 3: laminar (region 1), transitional (region 2) and turbulent (region 3). Viscous effects play an important role in the vicinity of the head-end ($0 < x/h < 1/\mathrm{Re}$, where the Reynolds number is based on the injection velocity). The flow is predominantly laminar in the upstream part of the channel ($0 < x/h < 5$) and undergoes transitions to turbulence as a result of hydrodynamic instability ($5 < x/h < 10$). Unlike channel flow with solid walls, the outbreak of turbulence occurs away from the walls (shaded region). The peak of turbulence intensity moves closer to the wall in the downstream direction until the surface injection prohibits further penetration of turbulence ($10 < x/h < 60$). As the flow develops farther downstream, the profile of axial velocity becomes much steeper near the wall, but flatter in the core region (near the centreline).

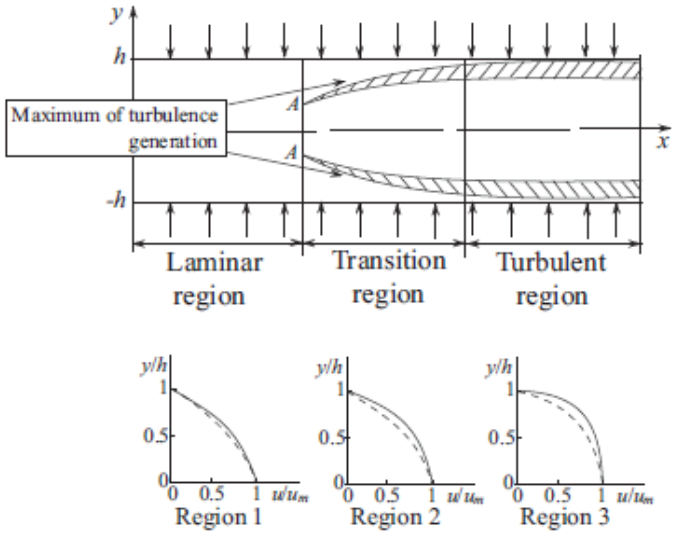

Figure 3. Flow regimes in channel with fluid injection

Profiles of axial velocity predicted with the developed model (solid lines) more flatter in the core region and more steeper in the near wall region than those in vortical flow (dashed lines). The profiles of radial velocity predicted with RANS and model of vortical flow are in a good agreement. Compressibility effects in the downstream part of the channel lead to small discrepancy of the results based on different models. Reynolds number has a small influence on profiles of axial and radial velocities in channel formed by wall injection.

5.2 Velocity

As the injection velocity increases, the influence of viscous effects on the turbulent flow structure becomes less pronounced and is mainly manifested in the axial region, leading to insignificant expansion of the velocity profile. As the Reynolds number increases, the axial velocity profile becomes more extended and tends to a cosine distribution in the case of intense injection from channel walls (Re $\rightarrow \infty$). The profile of axial velocity of the particulate phase is less filled as compared to the fluid velocity profile.

The profiles of the axial velocity of the gas and particulate phase in the channel for different particle Stokes numbers are shown in the Figure 4 (the results presented correspond to the dynamic equilibrium on the propellant surface). The results are normalized to the maximum fluid velocity in the channel, u_m, and the fluid injection velocity, v_w. The influence of the initial non-equilibrium conditions leads to modification of the particulate phase velocity profile near the injection surface.

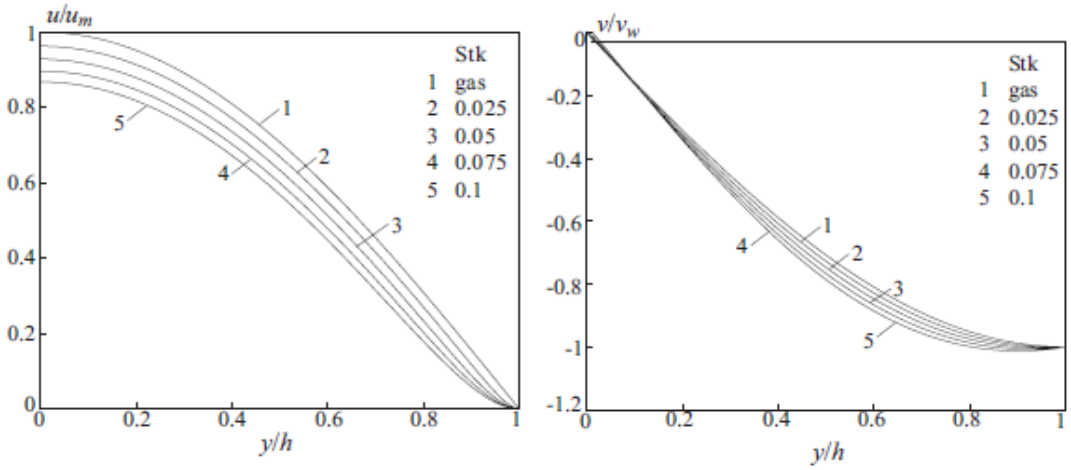

Figure 4. Profiles of the axial and radial velocities of gas and particles

5.3 Turbulence intensity

A negative pressure gradient due to flow acceleration exists in the injection-driven flow, which exerts an appreciable effect on the mechanism and intensity of turbulent transfer. Laminar to turbulent transition occurs further downstream (except for the near-wall and near-centreline regions), which is manifested in the presence of a turbulence front and displacement of the turbulent kinetic energy peak from the wall inward the flow. Near the channel wall, there is a layer with a low (tending to zero) of the turbulent kinetic energy (displacement zone). Near the injection wall and the channel centreline, the flow is virtually laminar. An increase in the level of turbulent velocity oscillations is observed in the strong shear region at a certain distance from the channel wall, where the fluid particles moving normal to the surface change the direction of their motion to the opposite one in a narrow subsurface layer.

Acoustic oscillations exert strong influence on unsteady flow evolution. In particular, single-harmonic oscillations excite a fluctuating flow with a broadband frequency spectrum [3] (this phenomenon is referred to as acoustically induced turbulent motion). Generation of turbulence by organized external forcing is viewed as an energy transfer process from the acoustic flowfield to the turbulent flowfield. The coupling between the Reynolds stresses and the gradient of acoustic velocity provides a mechanism to transfer the kinetic energy from acoustic motions to turbulent fluctuations. Furthermore, an early transition from laminar regime to turbulent one occurs depending on the forcing amplitude and frequency (Figure 3). The effect of energy exchange tends to be more profound for low-frequency acoustic oscillations.

The radial profiles of time-averaged axial velocity and turbulent kinetic energy at various axial locations (solid lines) are shown in the Figure 5 and Figure 6 for the first longitudinal mode ($f \sim 1000$ Hz, $\phi = 0.02$). Lines 1 correspond to the simulation of the injection-driven flow based on RANS equations and k–ε model, and lines 2 correspond to large-eddy simulation (LES) of channel flow induced by wall injection [23]. The profiles corresponding to steady state flow (dashed lines) are also included for comparison. An enhanced level of turbulence due to acoustic excitation is clearly observed. The acoustic waves induce flow instability and cause transfer of energy from the oscillatory organized to the turbulent field.

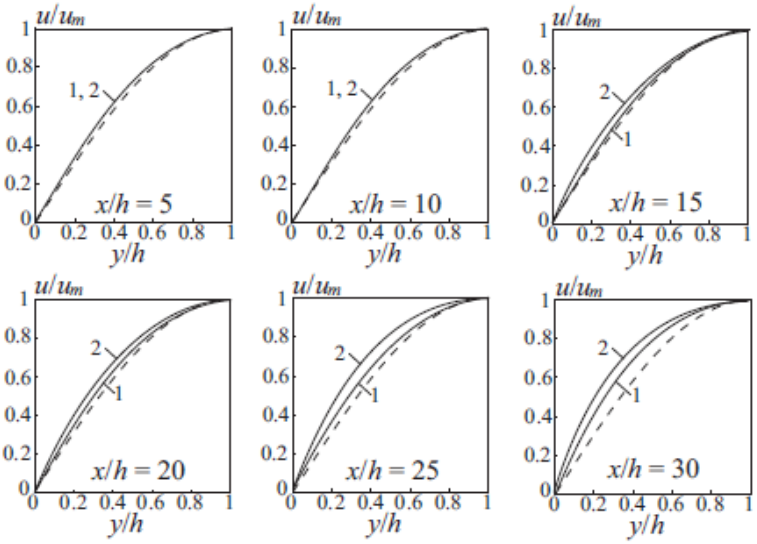

Figure 5. Radial profiles of axial velocity

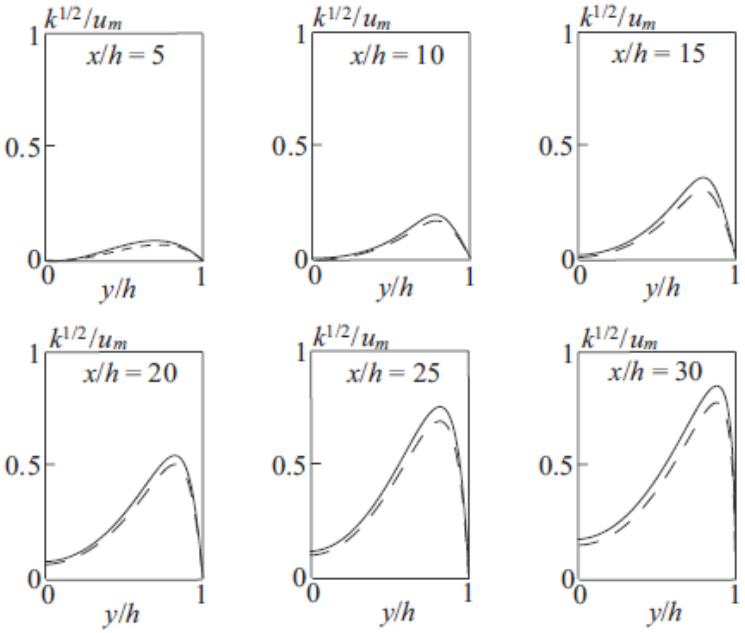

Figure 6. Radial profiles of turbulent kinetic energy

The particles exert a dual effect on the turbulence characteristics (Figure 7). On the one hand, additional (as compared to the turbulent flow of a pure gas) dissipation of the turbulent kinetic energy occur. On the other hand, the presence of particles decreases the boundary layer thickness, increasing the gradient of the mean fluid velocity near the wall, which leads to additional generation of turbulence.

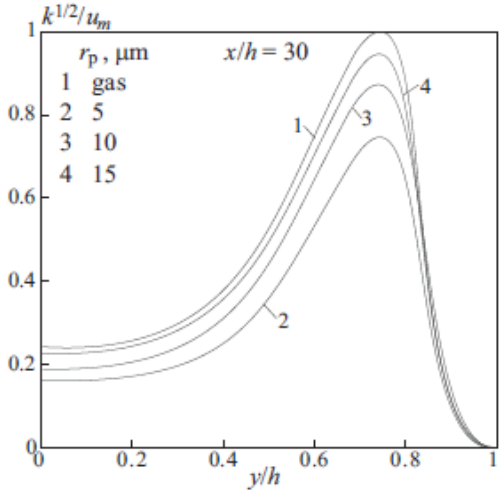

Figure 7. Radial profiles of turbulent kinetic energy

The influence of the particles on the turbulent flowfield is determined by the ratio of the time micro- and macro-scales of turbulence in different regions of the flow and by the particle relaxation time. The presence of two scales in the equations of the k–ε turbulence model is responsible for the different character of the particle effect depending on the particle Stokes number. The turbulizing effect of fine particles ($r_\mathrm{p} < 5\ \mu$m) moving almost in equilibrium with the gas is caused by a decrease in viscous dissipation. Not interacting with energy-intensive oscillations, such particles suppress the high-frequency part of the spectrum affecting the turbulent energy dissipation. A decrease in the turbulent kinetic energy due to injection of relatively coarse particles ($r_\mathrm{p} > 10\ \mu$m) into the flowfield is caused by additional dissipation resulting from momentum exchange and fluctuating slipping.

5.4 Attenuation and dispersion

Important factors in particle interaction with acoustic oscillations are acoustic Stokes number, mass concentration of particles, m_p, and the wavelength of acoustic oscillations, λ_a.

As a part of the model validation effort, the attenuation and dispersion of acoustic waves by particles in a channel flow is studied. The results have a good agreement with linear theory [17] in terms of attenuation coefficient and acoustic velocity as functions of frequency, particle relaxation time and mass fraction. In calculations, $\tau_a = 0.5$ ms, and $\tau_v = 0.1$ and 10.0 ms for fine particles ($d_\mathrm{p} = 10\ \mu$m) and coarse particles ($d_\mathrm{p} = 100\ \mu$m), respectively.

Particles are inclined to damp and to disperse the waves by slowing them. The damping is more pronounced when the particle relaxation time is close to the acoustic time period (the acoustic Stokes number is close to 1). The damping increases with the particles loading. The Figure 8a shows a good agreement of the spatial attenuation coefficient of the acoustic wave between the numerical calculations and the theory over a wide range of oscillation frequency, particle size and particle loading. There exists the optimum particle size at which the maximum damping of acoustic motion occurs. For small particles than closely follow the wave motions, the relative velocity and temperature differences between two phases become so small that the viscous and thermal dissipation is insignificant. The large particles hardly follow the wave motions to cause effective momentum and energy exchange, thereby leading to negligible acoustic attenuation. Only particles between these two extremes exert dissipation on wave motions. The Figure 8b shows particle dispersion effect. Propagation of acoustic waves in gas-particle flow involves a series of rarefaction and compression processes, during which both momentum and thermal relaxation take place between particles and gas.

For small particles, equilibrium is reached, and particles are treated as additional gas species. For large particles, the gas remains almost unchanged, and the acoustic wave speed has a value corresponding to that in a pure gas.

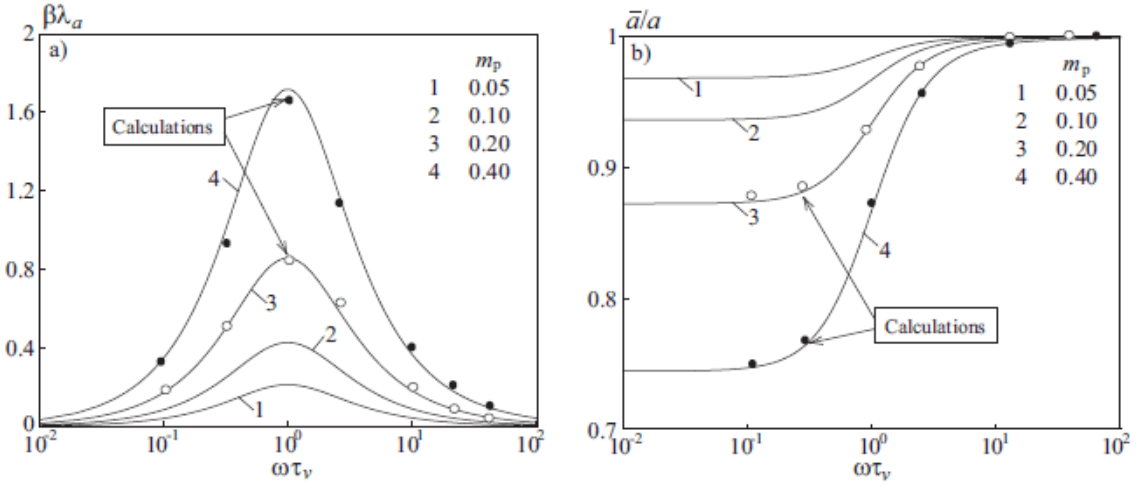

Figure 8. Spatial attenuation coefficient and particle dispersion effect

The specific acoustic impedance is a ratio of acoustic pressure to flow velocity. The acoustic impedance at a particular frequency indicates how much sound pressure is generated by a given gas vibration at that frequency. In gas-particle mixture, the acoustic impedance is defined using density of the mixture and speed of sound of the mixture. The acoustic impedance of the two-phase mixture has an approximately constant value in the entire range of the acoustic Stokes number parameter, $\omega\tau_v$, and is almost independent of the particle mass fraction. The effective parameters of the gas-particle mixture are presented as a sum of parameters corresponding to the pure gas and a correction caused by the presence of particles. In the case of low frequencies or fine particles ($\omega\tau_v \to 0$), the effective density of the mixture tends to its limiting value in the equilibrium flow, $\overline{\rho} = \rho(1 + m_\mathrm{p})$. In the case of high frequencies or coarse particles ($\omega\tau_v \to \infty$), the correction to density due to the presence of particles becomes negligibly small, therefore $\overline{\rho} = \rho$.

The optimal particle size (for $\omega\tau_v = 1$) that ensures the most significant damping of acoustic oscillations is determined. For fine particles, which are completely entrained into the wave motion and move almost in equilibrium with the gas, changing the thermo-physical characteristics of the mixture to the maximum extent, the relative velocity and temperature of the phases have small values, and the role of viscous and thermal dissipation is negligible. Fine particles exert the most appreciable damping effect at high frequencies of oscillations. For coarse particles, which are not entrained into the wave motion (frozen flow), the momentum and heat exchange with the gas is negligibly small, and no effect of these particles on acoustic oscillations in the channel is observed. Particles of intermediate size are responsible for dissipation of the energy of acoustic oscillations.

For small mass fractions of the particulate phase, the damping coefficient is described by the relation [17]

$$\beta = -\frac{C_m \omega}{2} \frac{\omega\tau_v}{1 + (\omega\tau_v)^2}.$$

The maximum value of the damping coefficient is observed at $\omega\tau_v = 1$, which corresponds to the optimal particle size $d_\mathrm{p}^* = 18\mu/(\rho\omega)$. In this case, $\beta_\mathrm{max} = -C_m\omega/4$. For aluminum oxide particles at the frequency of oscillations equal to 6000 Hz, the optimal particle size is 3.3 μm, and the damping coefficient is 10^{-8} s^{-1}. For the frequency of oscillations decreased to 500 Hz, the optimal particle size

is 11 μm, and the damping coefficient decreases to 1.6 s^{-1}.

5.5 Particle dynamics

As the ratio of the particle relaxation time to the acoustic time for fine particles is comparatively small (Stk → 0), they respond to the turbulent oscillations of the carrier flow velocity and, therefore, to changes in its parameters and follow the acoustic velocity fluctuations. Coarse particles (Stk → ∞) do not respond to the turbulent oscillations of the fluid flow velocity.

Particle trajectories are computed for different particle diameters. A difference exists between particle trajectories calculated from laminar and turbulent flow fields. Small particles deviate from their mean flow paths under the influence of gas flow oscillations and turbulent dispersion, and enhance interphase interactions. The dispersion of particles is controlled by the particle Stokes number. Limiting trajectory of particles where concentration of particles increases is clearly observed in the calculations (Figure 9). Dispersion of particles leads to increasing the particles residence time in the channel. The particle damping effect is defined by the particle loading and the ratio of particle relaxation time to turbulent time scale. The particles lead to damping of turbulent fluctuations and have laminarisation effect resulting in additional dissipation of turbulent kinetic energy due to relative motion of gas and particles. The turbulence modulation effect is more visible for small particles.

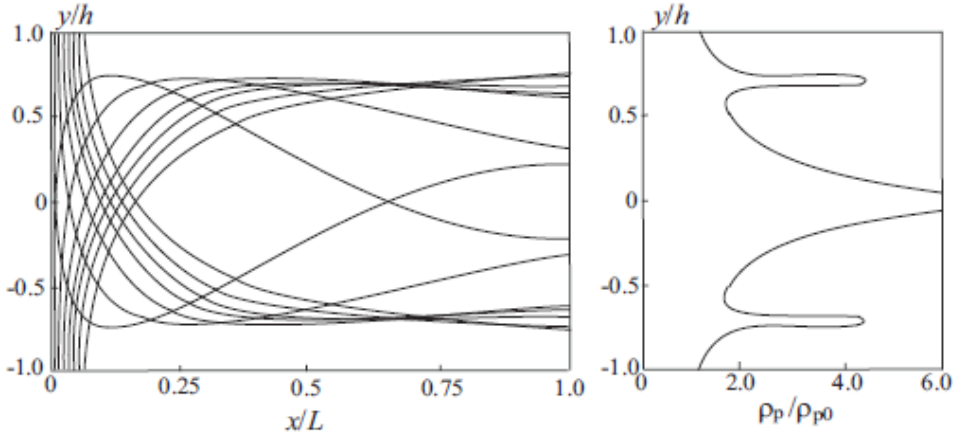

Figure 9.Particle trajectories and particle mass concentration for$d_{\mathrm{p}} = 20\mu$m

Figure 10 presents the trajectories of aluminum oxide particles ($r_{\mathrm{p}} = 5\text{–}50\mu$m) in an injection-driven flow ($v_w = 5$ m/s, $u_{\mathrm{p}w} = 0$ and $v_{\mathrm{p}w} = v_w$). The influence of the sluggishness of a particle on its scattering is inconclusive, since particles of different masses execute motion in different regions with a different turbulence intensity. The influence of velocity fluctuations on the particle motion is manifest when the particle gets into the turbulent region of the flow. A non-monotonic change in the turbulent kinetic energy along the axial coordinate leads to a non-monotonic change in the degree of particle involvement in the fluid flow, which is determined by the relation between the particle relaxation time and the turbulent time scale.

For particles of large fractions, velocity fluctuations produce no significant effect on the impurity motion throughout the region of flow development because of the inertia of such particles. Weak migration of particles towards decreasing turbulent kinetic energy is observed only for particles injected into the channel at a considerable distance from its head-end (at $x_{\mathrm{p}0} > 9$). Small particles are scattered rather strongly.

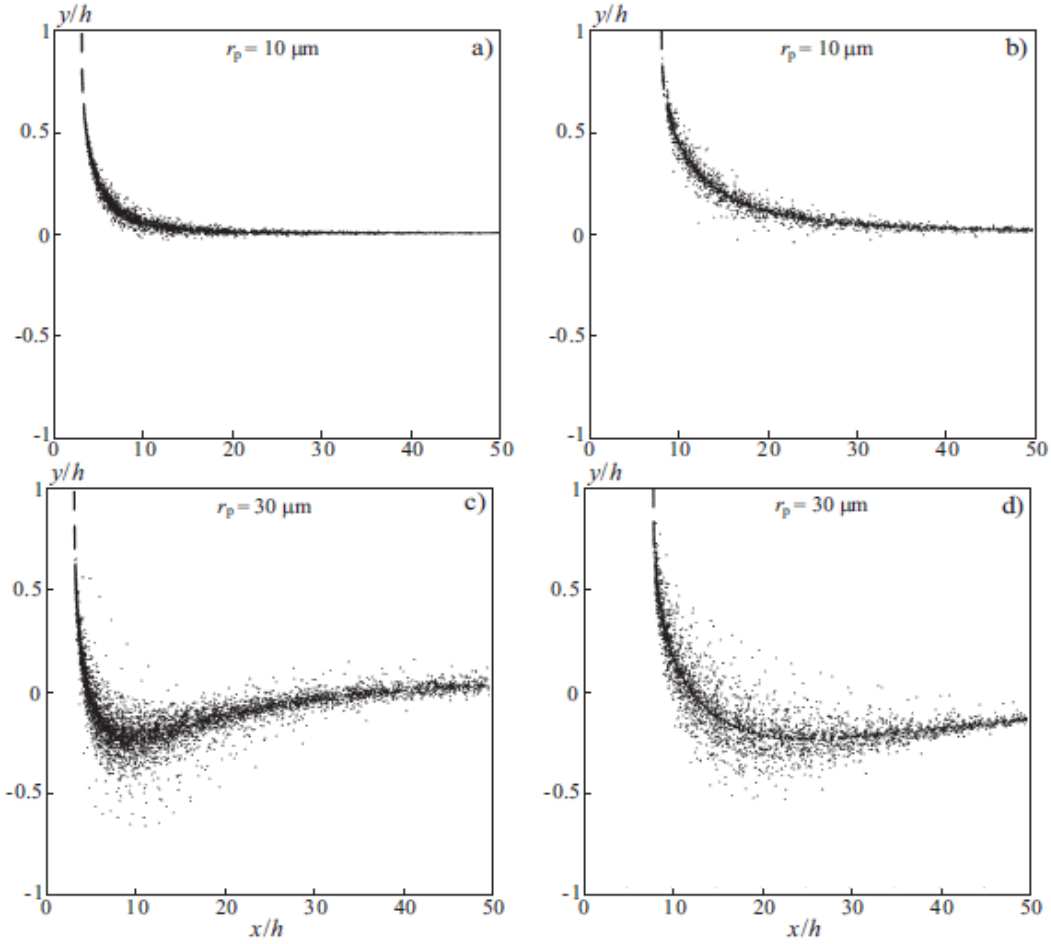

Figure 10. Trajectories of sample particles in the channel for$v_w = 5$ m/s

5.6 Acoustic and vortical flow fields

The oscillatory velocity field is split into acoustic and vortical flow motions. Several two-phase flow simulations are carried out to study the effects of the particle Stokes number on the oscillations behavior.

The Figure 11a shows the radial profiles of amplitude of axial velocity fluctuations (f~3770 Hz, $\phi = 0.02$) at the mid-section of channel (x/L~0.5) where flow is turbulent. The influence of large particles on the acoustic velocity is negligible because of their high inertia, and small particles effectively reduce the velocity oscillations. Turbulence exerts a small influence on the acoustic wave structure. Its primary contribution lies in the dissipation of the vortical motion through the turbulence-enhanced eddy viscosity. The Figure 11b shows results of the first longitudinal mode oscillations (f~943 Hz, $\phi = 0.02$). The damping effect of particles on the vortical flow motion is observed. An optimum size of particles corresponding to acoustic Stokes number close to unity is obtained to exert the maximum dissipation on flow oscillations.

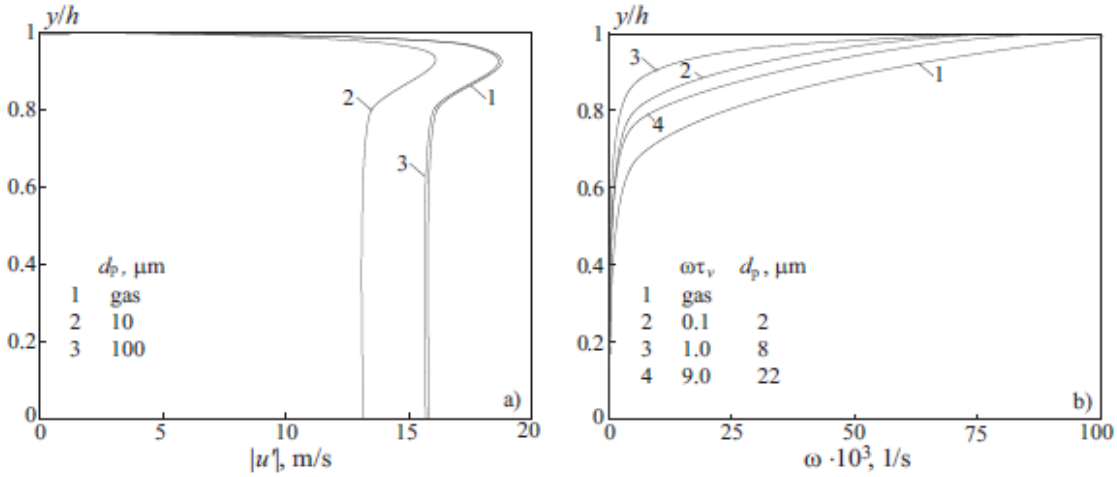

Figure 11. Effect of particles on acoustic and vortical flow fields for $m_{\mathrm{p}} = 0.2$

Figure 12 shows the radial profiles of the amplitude of axial velocity fluctuations in a laminar flow at a point located approximately in the middle of the channel ($x/L = 0.5$) for $f = 1885$ Hz and $\phi = 0.02$. The flow is laminar, the mass fraction of particles is assumed to be $m_{\mathrm{p}} = 0.2$, and the initial particle velocity is 0.1 m/s, which approximately corresponds to 10% of the injection velocity.

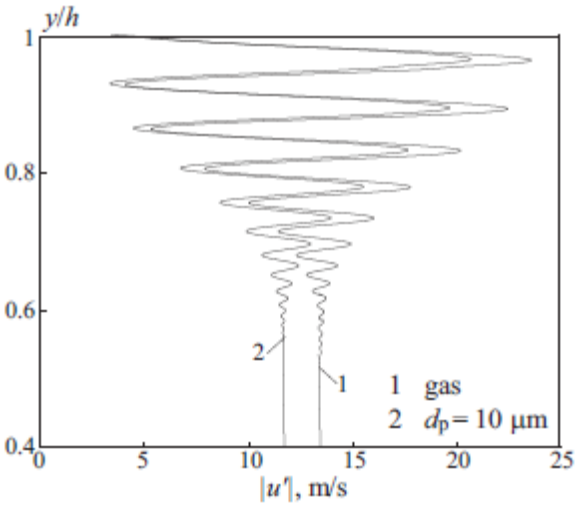

Figure 12. Radial profiles of the amplitude of axial velocity fluctuations

There are two characteristic flow regions. In the near-wall region of the flow ($y/h > 0.6$), there are significant oscillations of acoustic velocity and vorticity. In the axial region ($y/h < 0.6$), the vorticity waves decay because of viscous dissipation, and the influence of acoustic effects starts to dominate. The presence of particles leads to suppression of acoustic velocity fluctuations owing to momentum and energy exchange with the gas. The overall effect of the particulate phase is determined by the particle loading, dynamic and thermal particle relaxation times, and frequency of acoustic oscillations. Fine particles exert a significant effect on the acoustic flowfield, rapidly reaching equilibrium with the gas and effectively changing the density of the mixture, whereas coarse particles exert a minor effect. The maximum amplitude of axial velocity fluctuations is $|u'|_{\max} = 13.2$ m/s for $d_{\mathrm{p}} = 10\ \mu$m and $|u'|_{\max} = 15.5$ m/s for $d_{\mathrm{p}} = 100\ \mu$m (this value coincides with the corresponding value in the pure gas).

6 Conclusion

A numerical simulation of internal injection-driven turbulent gas-particle flow is performed with forced pressure oscillations. Flow unsteadiness is induced by forced periodic pressure oscillations at the channel head-end. The gas is simulated solving the RANS equations and equations of $k-\varepsilon$ turbulence model, and the particulate phase is treated with a Lagrangian model. The results obtained highlight the crucial significance of the particle dispersion in turbulent flowfield and high potential of statistical methods. Strong coupling between acoustic oscillations, vortical motion, turbulent fluctuations and particle dynamics is observed.

Particle trajectories are computed to assess the effects of the turbulent flowfield on the slag dispersion for different particle diameters. Turbulent dispersion is mainly observed for small particles. Dispersion of particles leads to increasing particle residence time and changes combustion efficiency. The ratio of particle relaxation time to acoustic characteristics time plays an important role in dictating the two-phase flow interactions with oscillatory internal flow. A maximum attenuation of acoustic waves occurs when those times are comparable. Small particles exert greater influence on the dispersion of acoustic wave through its effective modification of mixture compressibility.

Acoustic oscillations provide additional mechanism to energy transfer from periodic motion to turbulence leading to an enhanced level of turbulence and an early transition from laminar to turbulence. On the other hand, eddy viscosity tends to suppress vortical flow motion caused by acoustic waves. Fine particles (equilibrium flow) exert the most pronounced damping effect at high frequencies of oscillations. For coarse particles, which are not involved into the wave motion (frozen flow), momentum and heat exchange with the gas is negligibly small, and the effect of particles on acoustic oscillations in the channel is not observed.

References

1. Volkov K.N. Combustion of single aluminium droplet in two-phase flow. Heterogeneous Combustion. Nova Science, 2011, 191–260.
2. Dupays J. Two-phase unsteady flow in solid rocket motors. Aerospace Science and Technology, 2002, 6(6), 413–422.
3. Flandro G.A. Effects of vorticity on rocket combustion stability. Journal of Propulsion and Power, 1995, 11(4), 607–625.
4. Vuillot F. Vortex-shedding phenomena in solid rocket motors. Journal of Propulsion and Power, 1995, 11(4), 626–639.
5. Apte S.V., YangV. Unsteady flow evolution and combustion dynamics of homogeneous solid propellant in a rocket motor. Combustion and Flame, 2002, 131(1–2), 110–131.
6. Uskov V.N., Chernyshov M.V. Differential characteristics of the flow field in a plane overexpanded jet in the vicinity of the nozzle lip. Journal of Applied Mechanics and Technical Physics, 2006, 47(3), 366–376.
7. Silnikov M.V., Chernyshov M.V., Uskov V.N. Two-dimensional over-expanded jet flow parameters in supersonic nozzle lip vicinity. Acta Astronautica, 2014, 97, 38–41.
8. Silnikov M.V., Chernyshov M.V., Uskov V.N. Analytical solutions for Prandtl–Meyer wave – oblique shock overtaking interaction. Acta Astronautica, 2014, 99, 175–183.
9. Silnikov M.V., Chernyshov M.V. The interaction of Prandtl–Meyer wave and quasi-one-dimensional flow region. Acta Astronautica, 2015, 109, 248–253.
10. Cai W., MaF., YangV. Two-phase vorticoacoustic flow interactions in solid-propellant rocket motors. Journal of Propulsion and Power, 2003, 19(3), 385–396.
11. Culick F.E.C. The stability of one-dimensional motions in a rocket motor. Combustion Science and Technology,1973, 7(4), 165–175.
12. Betelin V.B., Smirnov N.N., Nikitin V.F., Dushin V.R., Kushnirenko A.G., Nerchenko V.A.,

Evaporation and ignition of droplets in combustion chambers modeling and simulation. Acta Astronautica, 2012, 70, 23–35.
13. Smirnov N.N., Betelin V.B., Kushnirenko A.G., Nikitin V.F., Dushin V.R., Nerchenko V.A. Ignition of fuel sprays by shock wave mathematical modeling and numerical simulation. ActaAstronautica, 2013, 87, 14–29.
14. Smirnov N.N., Nikitin V.F., Dushin V.R., Filippov Yu.G., Nerchenko V.A., Khadem J. Combustion onset in non-uniform dispersed mixtures. ActaAstronautica, 2015, 115, 94–101.
15. Dupays J., VuillotF. Propagation of acoustic waves in a two-phase vaporizing mixture. Journal of Propulsion and Power, 2002, 18(1), 222–224.
16. Brooks K.P., BecksteadM.W. Dynamics of aluminum combustion. Journal of Propulsion and Power, 1995, 11(4), 769–780.
17. Temkin S. Attenuation and dispersion of sound in dilute suspensions of spherical particles. Journal of Acoustical Society of America, 2000, 108(1), 126–146.
18. Volkov K. Internal turbulent two-phase flows formed by wall injection of fluid and particles. Proceedings of the 5th ECCOMAS Computational Fluid Dynamics Conference, 14–17 June 2010, Lisbon, Portugal, 01649.
19. Cousteix J., DesopperA., HoudevilleR. Structure and development of a turbulent boundary layer in an oscillating external flow. Proceedings of the First International Symposium on Turbulent Shear Flows, 18–20 April 1977, Pennsylvania State University, Pennsylvania, USA, 154–171.
20. Ramaprian B.R., TuS.W. An experimental study of oscillatory pipe flow at transitional Reynolds numbers. Journal of Fluid Mechanics, 1980, 100(3), 513–544.
21. Tseng I.-S., YangV. Combustion of a double-base homogeneous propellant in a rocket motor. Combustion and Flame, 1994, 96(4), 325–342.
22. Volkov K.N. Unstructured-grid finite-volume discretization of the Navier–Stokes equations based on high-resolution difference schemes. Computational Mathematics and Mathematical Physics, 2008, 48(7), 1181–1202.
23. Volkov K.N. Large-eddy simulation of free shear and wall-bounded turbulent flows. Atmospheric Turbulence, Meteorological Modelling and Aerodynamics. USA, Nova Science, 2010, 505–574.
24. Chakravarthy S.R., OsherS. A new class of high-accuracy TVD schemes for hyperbolic conservation laws. AIAA Paper, 85-0363.
25. Volkov K.N. Preconditioning of the Euler and Navier–Stokes equations in low-velocity flow simulation on unstructured grids. Computational Mathematics and Mathematical Physics, 2009, 49(8), 1789–1803.
26. Kourta A. Vortex shedding in segmented solid rocket motors. Journal of propulsion and power, 1996, 12(2), 371–376.
27. Emelyanov V.N., Karpenko A.G., Volkov K.N. Development of advanced computational fluid dynamics tools and their application to simulation of internal turbulent flows. Progress in Flight Physics, 2015, 7, 247–268.

Highlights

- A numerical analysis of the internal injection-driven turbulent gas-particle flow is performed
- Coupling between turbulence, vortical flowfield and particle dynamics is taken into account
- Acoustic oscillations provide additional mechanism to energy transfer from periodic motion to turbulence
- The results obtained highlight the crucial significance of particle dispersion in turbulent flowfield